Performance Enhancement of EAD Thrusters With Nonuniform Emitters Array

Davide Usuelli, Raffaello Terenzi, Stefano Trovato, and Marco Belan

***Abstract*— This work presents an experimental campaign to optimize the performance of electro-aerodynamic (EAD) thrusters through nonuniform emitter arrangements. The study examines the impact of emitter configurations on thrust and thrust-to-power coefficients C_T and C_{TP}. Different emitter arrangements, including collinear and staggered arrays, are tested using thrust, electrical, and velocity measurements as diagnostics. The tests are parametrically performed for different sizes (chords) of the collector electrodes. Results reveal that nonuniform emitter configurations outperform standard arrays, in particular, with short chord collectors, widely spaced apart. An optimal configuration for C_T is identified among the staggered ones. In addition, droplet collectors demonstrate competitive performance compared to airfoil collectors.**

***Index Terms*— Atmospheric ion thruster, corona discharge, EAD propulsion, ionic emitters configuration.**

I. Introduction

THE demand for sustainable aviation has driven worldwide researchers over the past decades to seek alternative propulsion methods to conventional aeronautical thermal engines [1], [2]. The current trend is to develop electrical propulsion systems to reduce pollutants and noise around airports and major cities. Historically, electric propulsion has been used in space applications such as in Hall thrusters [3], [4], [5], while electric-driven propellers are utilized for UAVs and small general aviation planes. A promising alternative to propellers is electro-aerodynamic (EAD) thrusters. These devices, characterized by their simple geometry, offer advantages such as zero emissions, low noise, and no moving parts, resulting in reduced maintenance requirements. Notable prototypes include airplane [6], which glided thrown by a slingshot, and ionocrafts [7], which lifted vertically with a wireless power supply on board and [8] which lifted from the ground with its own power supply on board. These prototypes, dating back a decade ago, demonstrated the feasibility of EAD technology.

An EAD thruster, in its simplest form, consists of two electrodes operating under a corona discharge regime: the emitter—where air ionization occurs—and the collector. The electrodes are supplied with a high-voltage source, creating an intense electric field that promotes ionization near the emitter and drifts ions toward the collector [9], [10]. The ion emitter is, in general, characterized by a small cross section: wires with a diameter below 200 μm are often employed, however, other geometries such as blades [11], [12], [13] and pins [14], [15], [16] are also found in the literature. The collector unit features a greater dimension, with airfoils [6], cylinders [17], and droplets [7] being the adopted geometries: several studies involving their optimization can be found in [18], [19], and [20]. The generated thrust (T) results from the interaction between drifting ions and neutral molecules, which exchange momentum during collisions. A basic EAD thruster consists of a single emitter and collector, forming a thruster unit. Thruster arrays can be generated by stacking units in parallel [19], [21] or aligning them sequentially to form multistaged thrusters [20], [22]. The spatial arrangement of electrodes is still subject to investigation, leading to different concepts. Studies in the literature focus on optimizing the distance between collectors SC and the distance between electrodes of opposed polarity d for given voltage and electrode shapes. Given that this technology is still in its early stages of development, there is significant room for improvement. One of the open fields of investigation is the arrangement of emitters, such as increasing their density [23], which proportionally enhances multiple performance parameters until the occurrence of the shielding phenomenon, leading to performance degradation [24], [25]. In general, EAD thrusters operate using a dc voltage supply for the corona discharge; however, different ionization sources can be employed, such as DBD [26], [27], which exploits the ac regime, or nanosecond pulsed power supplies, capable of generating an increased number of ions before breakdown occurs [28], [29]. Thrusters have been tested both on the bench and in wind tunnels to investigate the effects of an asymptotic flow [30], [31]. The performances of an EAD thruster are typically evaluated considering the T, power consumption (P), thrust-to-power ratio (T/P) as an efficiency index and thrust density (T/A) as a compactness index, with A being the reference frontal area. The promising performance of EAD thrusters has also attracted interest from airship designers [32] for potential low-cost alternatives to satellites.

This work aims at enhancing the performance of an EAD thruster by further expanding the research on the spatial configuration of emitters, in particular, exploiting nonuniform arrays. First, the existing configuration for a typical

Received 3 August 2024; revised 7 November 2024 and 15 November 2024; accepted 21 November 2024. The review of this article was arranged by Senior Editor S. J. Gitomer. *(Corresponding author: Davide Usuelli.)*

The authors are with are with the Department of Aerospace Science and Technology (DAER), Politecnico di Milano, 20156 Milan, Italy (e-mail: davide.usuelli@polimi.it).

Color versions of one or more figures in this article are available at https://doi.org/10.1109/TPS.2024.3505980.

Digital Object Identifier 10.1109/TPS.2024.3505980

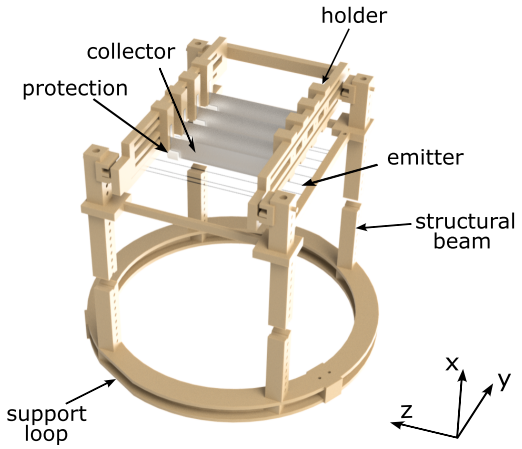

Fig. 1. Experimental rig.

wire-to-airfoil propulsive system is analyzed, and then new arrangements are investigated. Thrust, electrical, and velocity measurements are analyzed and used as diagnostics. To limit the variable's space, some constraints are imposed on the geometry.

This article is organized as follows. In Section II, the experimental setup is presented and the measurement techniques are discussed. Section III illustrates the design of the experiment along with the performance coefficients. Section IV presents the results of the experimental campaign, while Section V concludes the article.

II. Experimental Setup

Two experimental setups were employed in this study for thrust and velocity measurements using a precision balance and a Pitot probe. The test rig, previously utilized in [12] and [23], features components largely produced via rapid prototyping using acrylic styrene acrylonitrile (ASA). It consists of three main parts: the emitter frame, the collector frame, and structural beams as shown in Fig. 1.

Constantan wires with a diameter of 30 μm act as emitters. A long wire is wound around lateral arrays of pegs to form an array of parallel emitters. The spacing SE between the emitters is adjustable, starting from a minimum of 2.5 mm. Emitters are connected to a positive, dc high-voltage power supply. On the collector frame, holders are designed to accommodate various geometries. Four collectors are mounted in each test, as shown in the figure, which include airfoil and droplet geometries with variable thickness t and chord c. Each collector is coated with a 70-μm-thick aluminum foil and is electrically grounded. Insulating caps protect the ends of the collectors that face the emitters, to prevent reverse corona and early streamer formation due to the electric field intensity in this area. The collector holder allows for adjustable spacing between electrodes SC starting from a minimum of 10 mm.

Structural beams connect all components, providing additional design flexibility and ensuring precise distances between the electrodes in all directions. Vertical bars feature holes where the collector frame can be attached, enabling modification of the gap d between emitters and collectors in steps of 10 mm. The additional stiffness is provided by a support loop at the base of the setup, which is also used to transfer the load to the balance.

Detailed geometrical information and dimensions are provided in Section III.

A. Thrust Measurement

Thrust measurement is the main technique used in this experimental campaign to characterize the performances of the thruster's different configurations. The setup described above is positioned on top of a precision balance, characterized by a 0.1-mN accuracy. Structural beams ensure adequate spacing between electrodes and the balance plate to prevent electrostatic interference, and an additional grounded plate is placed on top of the balance for the same reason. In all experiments, the distance between the downward-facing emitters and the balance plate is always greater than 400 mm.

B. Velocity Measurement

Velocity measurements exploit the same setup described above. Minor modifications are implemented to guarantee alignment with respect to the probe. A Pyrex Pitot probe with a diameter of 1.2 mm is positioned on a plane 2 mm downstream of the trailing edges of the collectors as shown in Fig. 3. The probe position along the measurement plane is maneuvered using a motorized linear positioning device with an accuracy of ± 5 μm.

The pressure signal is acquired along the electrode spacing direction with a step of 0.5 mm in the vicinity of the collector's trailing edges, due to the high gradients present within the wake, and 1 mm in other regions. The pressure difference between the probe and the surrounding ambient is measured by a differential pressure transducer with a range from 0 to 20 Pa and an accuracy of 0.01% of the full scale.

C. Electrical Measurement

The electrical scheme of the setup is shown in Fig. 2. Both setups share the same high-voltage power supply which provides a positive dc voltage $V_s = 20 \pm 0.03$ kV. A ballast resistance $R_b = 0.996 \pm 0.003$ MΩ has been introduced for safety purposes. During the tests, corona voltage V_c and current i_c across the electrodes are measured. The former is acquired using a voltage divider with $R_{\text{tot}} = 47 \pm 0.001$ MΩ, while the latter is obtained from the voltage signal read across an $R_s = 88.5 \pm 0.01$ Ω shunt resistor.

D. Data Acquisition

During the thrust measurement, the thrust T is determined by the difference in the balance output reading when the thrust is switched on and off. For each test, acquisitions are averaged to obtain the final values, while the uncertainty is propagated using the root sum of squares (RSS) method. Thrust, V_c, and i_c are acquired using an oscilloscope with an acquisition time of 2 s and sampling frequency of 50 kS/s.

The velocity measurement primarily aims to investigate flow topology. Therefore, only the signal from the pressure transducer is acquired, with an acquisition time of 10 s and

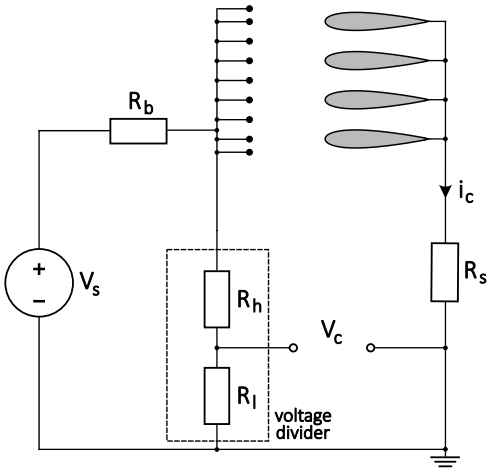

Fig. 2. Electrical scheme.

sampling frequency of 10 kS/s. Other electrical quantities such as the current and voltage at the power source are monitored to ensure the proper operation of the setup. The velocity u downstream to the collectors is calculated using the formula

$$u = \sqrt{\frac{2\Delta P}{\rho}} \tag{1}$$

where ΔP is the differential pressure measured by the transducer and ρ is the atmospheric density estimated using perfect gas law.

III. Design of the Experiment

A. Geometry Definition

Due to the considerable number of parameters that characterize the electrode configuration of EAD thrusters, some constraints based on consolidated results from the literature are introduced, limiting the number of variables for this work to focus predominantly on the emitter's placement. The considered parameters and their respective values are listed below and shown in Fig. 3.

1) Gap between the electrodes: $d = 20$ mm.
2) Spacing between collectors: SC $= 25, 35$ mm.
3) Collectors chord length: $c = 15, 20, 25, 100$ mm.
4) Collectors thickness-to-chord ratio: $t/c = 24\%$.
5) Collectors span: $b = 120$ mm.

Fig. 3 also introduces the nomenclature for the regions (cells) between and outside collectors. Concerning the test campaign, two symmetrical collector shapes are selected: airfoils and droplets. Airfoils are based on four-digit NACA shapes, properly scaled according to the selected chord and thickness; droplets feature a semicircular leading edge with a radius $r = t/2$.

The present work focuses on the emitter arrangement: the five examined configurations are depicted in Fig. 3. The reasons behind the choice of these particular configurations are exposed in Section IV. The first emitter disposition, referred to as the *single* configuration, presents an equal number of anodes and cathodes, that is, a 1:1 ratio, and it corresponds to the configuration most commonly found in [6], [7], and [17]. In the *hybrid* configuration, the number of emitters is doubled, with additional emitters placed at the extremities of the thruster (as in the case of [23]). However, in this case, the outer emitters may feature a different spacing in millimeters, denoted as h, compared to the inner anodes, thus leading to nonuniform dispositions. The two arrangements described above are said to be collinear since each collector directly faces an emitter. A different solution involves staggered arrays: in this case, each collector is paired with two emitters that are displaced at an equal distance from the collector axis creating a thruster unit; the resulting spacing in millimeters is denoted as H and these configurations are referred to as STG * (i.e., staggered), where * is the H value.

TABLE I
Performance Parameters and Dimensionless Coefficients

	Symbol	Ref. value from [18]	Coefficient
Thrust	$\frac{T}{b}$	$\epsilon\frac{V_c^2}{d}$	C_T
Thrust-to-Power	$\frac{T}{P}$	$\frac{d}{\mu_q V_c}$	C_{TP}

B. Performance Coefficients

The experimental data are analyzed to generate performance indicators, useful for comparing the results deriving from the different configurations. In literature, three performance parameters are generally adopted: T, T/P, and T/A. Depending on the optimization target, these parameters can be exploited to generate Pareto fronts for tradeoff analyses. In this work, T and T/P are the main outputs of interest: to provide meaningful comparisons with other setups, their dimensionless counterparts are introduced. The complete derivation can be found in [18]: the respective coefficients for T and T/P are reported in Table I, where ϵ is the permittivity and μ_q is the ion mobility. Each coefficient is obtained by dividing the dimensional data by the corresponding reference value.

IV. Results

A. Performance for $c = 100$-mm Collectors

The starting point of this work derives from the analysis contained in [23], where NACA0010 airfoil collectors with a 100-mm chord were arranged at a spacing of 25 and 35 mm and a gap $d = 20$ mm. The smaller one, for which spacing and gap are similar, yields a better T/A, while a higher spacing-to-gap ratio, such as for the 35-mm case, provides greater thrust and thrust-to-power overall. A condition in which the spacing is much smaller than the gap has not been considered as it has been proved to work inefficiently due to its inherently higher aerodynamic blockage [19]. In this work, both spacings are considered short-chord collectors and have never been tested together with an increased number of emitters.

Different uniform emitter arrangements were tested. The optimal configuration in [23] was the one identified as SC35 SE17.5, where the designation indicates a collector spacing SC $= 35$ mm and an emitter spacing SE $= 17.5$ mm, that is, the collector spacing is twice the emitter spacing. It features extremity emitters outside the reference area of the thruster, defined as the area limited by the first and last collectors,

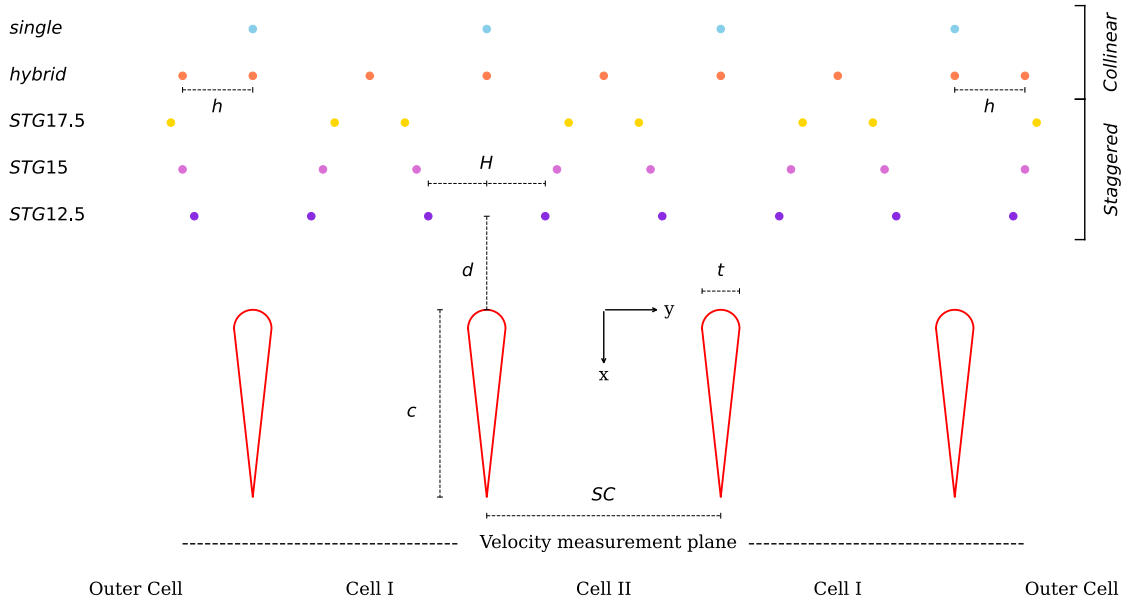

Fig. 3. Geometrical definition and nomenclature, not to scale.

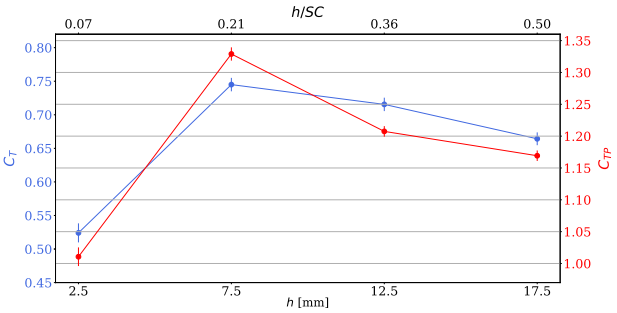

Fig. 4. Effect of h on performances of *hybrid* configuration. Data from [23] are scaled to obtain dimensionless coefficients.

with an external displacement $h = \mathrm{SC}/2$ (see Fig. 3). The first investigation in the present work focused on the effect of h on the thruster's performance. It is reasonable to believe that reducing the distance between the external emitter and the first and last collectors may improve performance due to an increase in the corona discharge intensity.

The range of h was selected according to the available spacing of pegs on the emitter-base: $h = 2.5, 7.5, 12.5, 17.5$ mm. The test rig is placed on top of the balance to read the thrust T, while V_c and i_c are acquired to generate performance coefficients for each configuration. Tests demonstrate that the configuration with SC25 does not significantly improve performance with extra emitters. Therefore, only results for SC35 are presented. As illustrated in Fig. 4, the optimal configuration for both T and T/P corresponds to the one with $h = 7.5$ mm referred to as *hybrid*, as a result of the compromise between the electrical shielding dictated by the proximity of the anodes and the distance between electrodes of different polarities. The respective performance enhancement compared to the SC35 SE17.5 case from [23] is shown in Table II.

To investigate the reasons behind the observed increase in the propulsive force, velocity measurements were performed along the spacing direction SC across all the thruster units.

TABLE II
COMPARISON BETWEEN SC35 SE17.5 AND *Hybrid*

	$SC35SE17.5$	*hybrid*
T	63.5 mN	71.22 mN (+12%)
T/P	4.95 N/kW	5.63 N/kW (+13%)

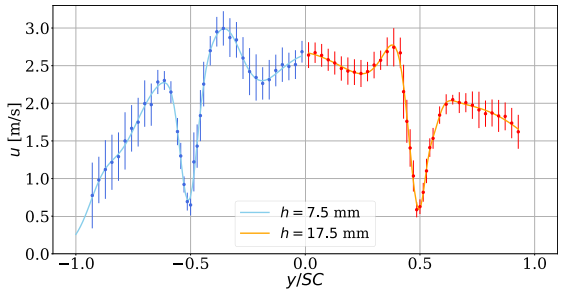

Fig. 5. Velocity profiles comparison between $h = 7.5$ mm and $h = 17.5$ mm. The range $0 < |y/\mathrm{SC}| < 0.5$ represents the outer half of Cell 1, while $0.5 < |y/\mathrm{SC}| < 1.0$ encompasses the outer cell, with the outermost collector being positioned at $|y/\mathrm{SC}| = 0.5$.

The comparison of velocity profiles between the *hybrid* case and the SC35 SE17.5 configuration is shown in Fig. 5. In particular, only the region of the outermost collector is illustrated, as the flow fields in the central cells do not present significant differences.

In the outer cell region, the *hybrid* arrangement shows a steeper velocity decay due to a shorter distance of the external emitter with respect to the cathode. Inside the cell, a higher velocity peak in the vicinity of the trailing edge is encountered. The acceleration may derive from a nonnull angle of attack of the airflow entering the cell due to the ionic wind generated by the external wire and conveyed into the cell (showing the typical flow pattern of the lee side of an airfoil), unlike the case of SC35 SE17.5 where a greater distance along the spacing direction prevents the increase in velocity.

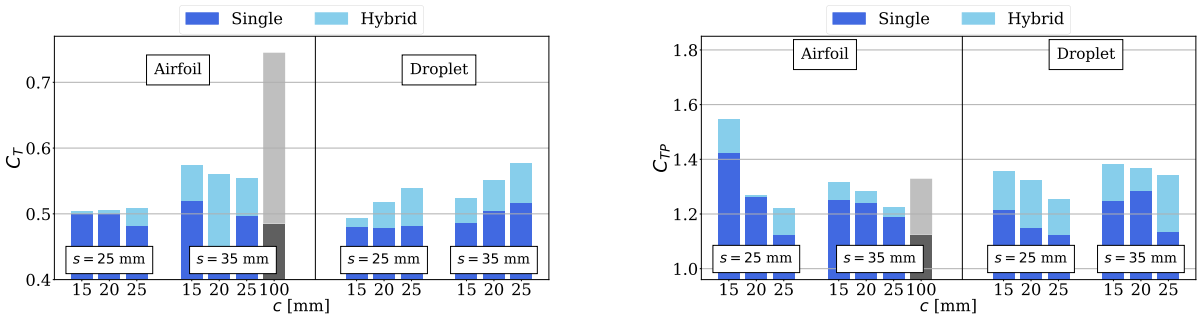

(a) (b)

Fig. 6. Performance comparison of *single* and *hybrid* configurations. Data for C100 airfoils from previous work are reported for comparison. (a) C_T. (b) C_{TP}.

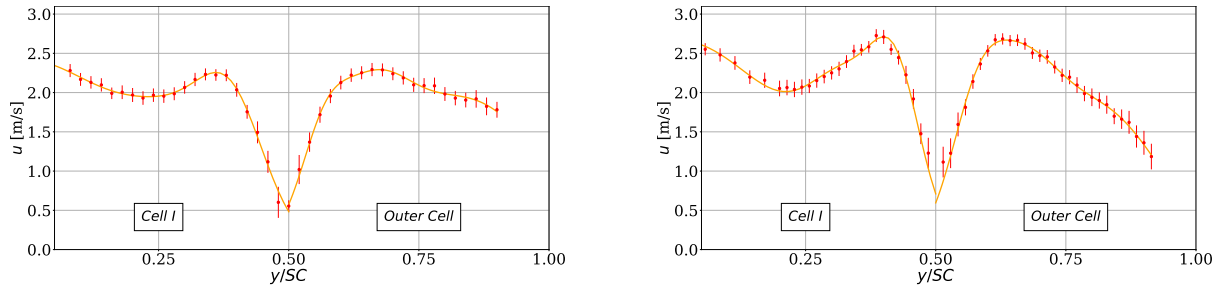

(a) (b)

Fig. 7. Velocity profiles for *hybrid* configurations with $c = 25$-mm airfoil collectors and different collector spacings SC. (a) SC25. (b) SC35.

TABLE III
VARIABLE SPACE

SC	$25, 35$ mm
c	$15, 20, 25$ mm
t/c	24%
Emitters	*single*, *hybrid*, *staggered*
Collectors	Airfoil, Droplet

Recent advancements in geometry optimization of EAD thrusters have demonstrated that collectors characterized by smaller chords c are beneficial for certain performance parameters, as smaller surfaces are exposed to the airflow [18].

In this work, the applicability of *hybrid* configurations to smaller collectors is questioned, as in [18] only *single* arrangements are tested.

B. Hybrid Configuration on Short-Chord Collectors

The accounted variables of the experimental campaign of this section and their possible values are listed in Table III.

An airfoil with $c = 25$ mm and $t = 6$ mm, which corresponds to $t/c = 24\%$, serves as the baseline geometry, as it is the optimum configuration from [18] for C_T and C_{TP}. Contrary to that study, in this work, the thickness-to-chord ratio is set constant while the chord length c is variable but excluding large values with respect to the gap d, as the latter determines noticeable changes in the performance parameters. While airfoil-shaped collectors have proved to perform well, droplet collectors have historically been used, that is, [7], [19], due to their satisfactory electrical performance. Additionally, a direct comparison between the two cross sections has never been performed for small chords.

The results are reported in Fig. 6, where the $c = 100$ mm NACA0010 airfoil presented at the beginning of the Results section is displayed in gray for a thorough comparison.

Each *hybrid* configuration outperforms the corresponding *single* arrangement. For the airfoil-shaped collectors, a smaller chord length leads to higher C_T while the trend is the opposite for droplet collectors. As the size of the collectors decreases, the gain in performance provided by the *hybrid* disposition is generally reduced. The $c = 100$ mm collectors still yield the highest value of C_T for the *hybrid* case. As shown in Fig. 5, the introduction of external emitters in a thruster with long chord collectors creates a beneficial extra velocity on the lee side of the outer collectors. As shown below, this advantage is reduced when using short collectors; however, long collectors turn out to be much heavier, limiting their use for viable applications, thus they are excluded from further considerations in the following sections. As a consequence, this study exclusively focuses on short-chord collectors. As a general trend for C_{TP}, smaller chords lead to higher values: this behavior is confirmed for all geometries.

The limited increase in performance provided by the *hybrid* arrangement suggests that this emitter configuration is less effective on small collectors. To assess the presence of the same phenomenon described above, velocity measurements are performed downstream of the thruster cells, focusing on the velocity peak that arises in the vicinity of the external collectors.

Fig. 7 shows the flow field downstream of Cell I and outer cell, for both SC25 and SC35 spacings between airfoil collectors. The comparison with Fig. 5 shows no remarkable distinction in the internal and external velocity profiles, which instead are very different when the chord is long. Here, they remain symmetrical across the external collectors without the presence of noticeable peaks, thus determining the lower

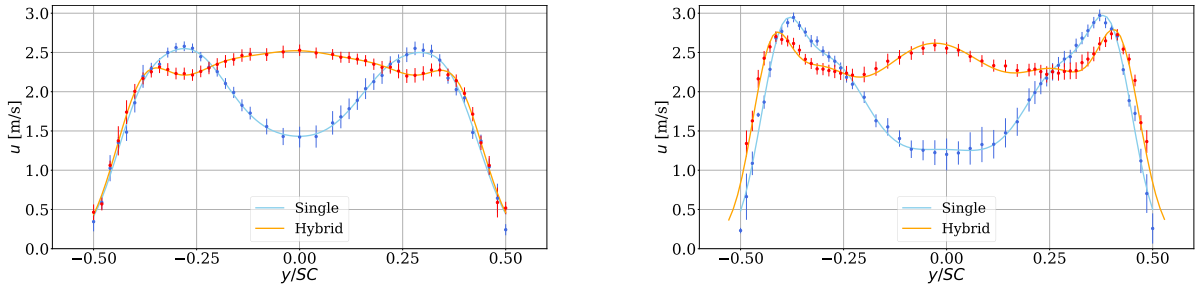

Fig. 8. Flow fields comparison in the central region downstream Cell II with $c = 25$ mm airfoil collectors, for different SC values. The presence of multiple emitters introduces additional peaks in velocity profiles. (a) SC25. (b) SC35.

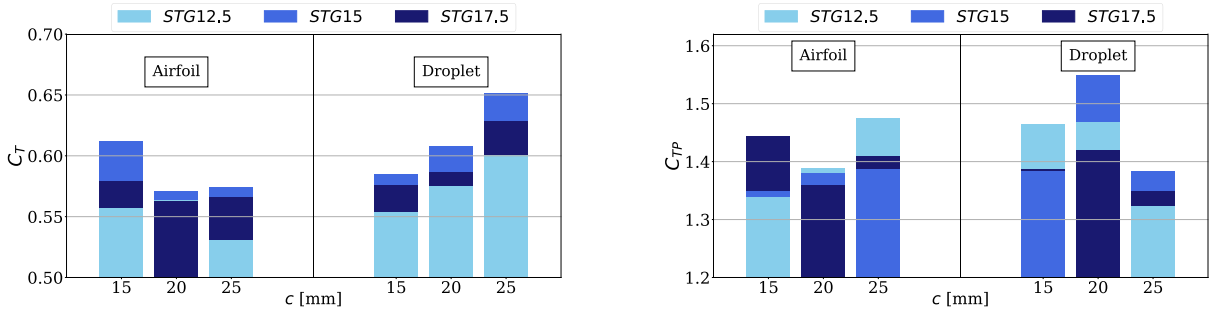

Fig. 9. Performance comparison between staggered configurations. The STG15 arrangement provides the highest values for C_T, while all staggered configurations deliver similar performances in terms of C_{TP}. (a) C_T. (b) C_{TP}.

effectiveness of the *hybrid* arrangement for minor chords when compared to the $c = 100$-mm collectors.

A significant difference for single configurations can be spotted between the Cell II flow fields shown in [23] and those of this work. Since Cell II is at the center of the thruster, it mimics periodic conditions as it is less affected by the edge effect. In the case of [23], there is a clear distinction between the flow fields associated with the different spacings, with SC25 being channel-like and SC35 being double jet-like flows. This differentiation is no longer evident with shorter chords as shown in Fig. 8, with the flow field being more similar to two distinctive jets developing close to the collector's wakes. The behavior change can be explained by considering the thickness-to-spacing ratio t/SC: all the tested geometries in this work are characterized by t/SC values that are closer to the one relative to the $c = 100$-mm airfoils at SC35, where the mutual influence between adjacent collectors is not substantial with respect to the cases where SC is equal to 25 mm. In other words, short collectors are not extended enough to create a channel flow between them.

C. Staggered Emitter Arrangement

The introduction of *hybrid* configurations did not result in a significant increase in performances for smaller collectors. The emitter arrangements considered above are characterized by a collinear alignment, where each collector is facing one emitter. In literature, several examples of staggered arrays such as those in [7] and [23] have proved to be beneficial, especially when considering T/P.

Due to the nearly isolated behavior of each collector at small chords for the tested spacings, it is reasonable to believe that an increase of the emitter density only on the proximity of the cathodes could overcome the limits that the *hybrid* disposition encountered instead. Previous analyses have shown how configurations with SC35 consistently outperform those with SC25. Therefore, only the former is considered in this investigation. The parameter to be optimized is H, defined as in Fig. 3. According to the previously introduced nomenclature, the tested configurations are: STG12.5, STG15, and STG17.5, meaning $H = 12.5, 15, 17.5$ mm, respectively. The lower and upper limits are selected based on shielding effects and collector spacing, respectively, as well as the constraints imposed by the experimental setup.

In the staggered configurations, only two emitters per collector are placed since increasing the number with small spacings may easily lead to electric shielding while increasing the spacing leads to performance degradation. The results in terms of C_T and C_{TP} are shown in Fig. 9.

The histogram plot illustrates that the STG15 configuration is the one providing the highest thrust coefficients C_T for both airfoil and droplet collectors. Increasing or reducing the chord length leads to the same trend of Fig. 6 for airfoils and droplets, respectively. Moreover, this staggered configuration always outperforms the *hybrid*. Regarding C_{TP}, nonuniform arrays exhibit higher values with respect to the *hybrid* as expected, due to the greater average distance between the electrodes in the proximity of the collectors. However, unlike for the case of thrust coefficient C_T, no single staggered configuration consistently provides the highest values for each type of collector, with their variations being limited.

D. Pareto Front

The experimental results have been presented in the previous subsections following a logical flow from simple

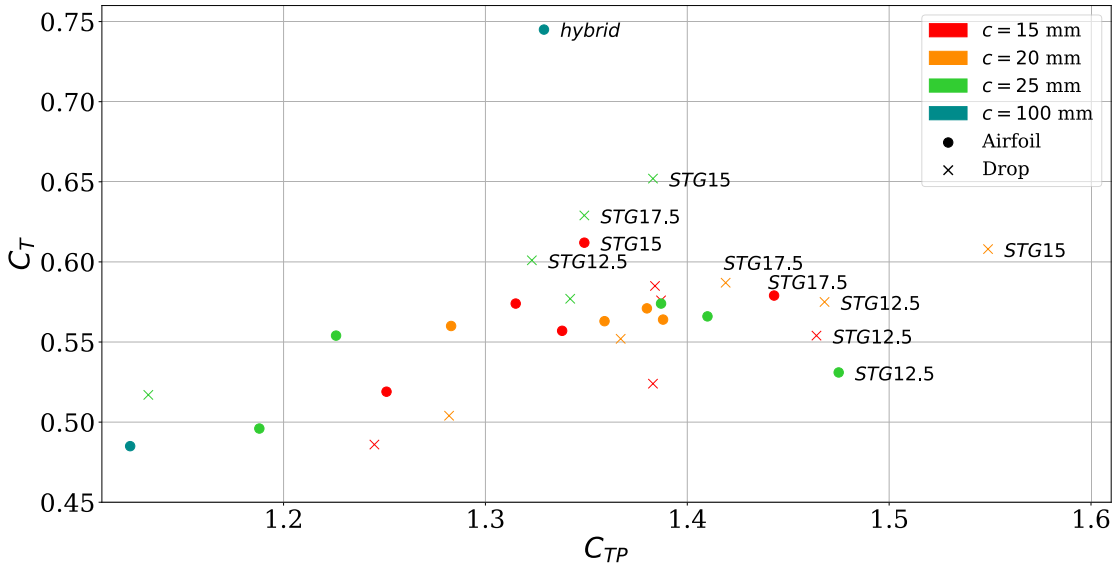

Fig. 10. Pareto front: C_T and C_{TP} are the selected parameters of interest. STG configurations outperform *single* and *hybrid* as more emitters per collector are present while limiting the P due to their disposition. Emitter arrangements are explicitly labeled only at the outermost front.

geometries to complex arrangements, to increasingly improve the overall propulsive performance. To globally visualize the results from the extensive campaign and conclude, a Pareto front is generated considering C_T and C_{TP} as the selected nondimensional variables. Since the configurations with 35-mm collectors spacing are the ones providing the best performances compared to their respective SC25 cases, the Pareto front in Fig. 10 considers only the configurations featuring the former spacing.

Except for the heavy 100-mm airfoil chord case, which was added only for comparison purposes, the outermost front for smaller chords is made up of staggered configurations. These offer the best compromise between T and P, making them the preferred choices for propulsive applications with small and light collectors.

V. Conclusion

This work aimed to explore the performance enhancement of EAD thrusters through several emitter configurations. Initial results indicate that using a hybrid configuration with collinear emitter arrangements can significantly improve the thrust and T/P, with an increase of up to 12% and 13%, respectively, for long-chord collectors. However, by decreasing the cathode dimensions, the performance gains are less pronounced. The analysis revealed that the flow field differences between hybrid and single-emitter configurations diminish with shorter collectors, reducing the effectiveness of hybrid dispositions.

Further development leads to the introduction of staggered arrays. These outperform all the previous configurations, showing performance increases for both C_T and C_{TP}. The choice of employing dimensionless coefficients has allowed us to compare different configurations and find a global optimum while operating at a single voltage and without varying the geometrical gap between the electrodes, therefore resulting in valid also for scaling purposes. This remains true as long as the 1-D theory underpinning the derivation of dimensionless coefficients is valid. In particular, this entails a gap between the electrodes that is much larger than the thickness of the collectors and collectors much thinner than their spacing, therefore limiting the influence of the transverse dimension (y) of the 2-D geometry. The STG15 arrangement provides the highest values for C_T, while all staggered configurations deliver similar performances in terms of C_{TP}. In general, a 35-mm collector spacing in the order of twice the electrode gap provides the best performance.

The Pareto front suggests that droplet collectors are a competitive geometry compared to airfoils as their worse aerodynamic characteristics are compensated by better electrical performances.

All the tests were performed on a bench, future developments would, therefore, require extending the experimental investigation to wind tunnel testing, where a nonnull asymptotic velocity can shift the optima found in this work. Due to the considerable number of geometric variables, numerical support may help identify the most performing configurations, optimizing the geometry to reduce aerodynamic drag while maintaining high electrical performances.

Data Availability Statement

All data required to reproduce the results and figures presented in this article are publicly available at Zenodo under the DOI: https://doi.org/10.5281/zenodo.14202884.

References

[1] W. Cao, B. C. Mecrow, G. J. Atkinson, J. W. Bennett, and D. J. Atkinson, "Overview of electric motor technologies used for more electric aircraft (MEA)," *IEEE Trans. Ind. Electron.*, vol. 59, no. 9, pp. 3523–3531, Sep. 2012.

[2] B. J. Brelje and J. R. Martins, "Electric, hybrid, and turboelectric fixed-wing aircraft: A review of concepts, models, and design approaches," *Progr. Aerosp. Sci.*, vol. 104, pp. 1–19, Jan. 2019.

[3] D. M. Goebel and I. Katz, *Fundamentals of Electric Propulsion: Ion and Hall Thrusters*. Hoboken, NJ, USA: Wiley, 2008.

[4] S. Mazouffre, "Electric propulsion for satellites and spacecraft: Established technologies and novel approaches," *Plasma Sources Sci. Technol.*, vol. 25, no. 3, Jun. 2016, Art. no. 033002.

[5] C. Charles, "Plasmas for spacecraft propulsion," *J. Phys. D: Appl. Phys.*, vol. 42, no. 16, Aug. 2009, Art. no. 163001.
[6] H. Xu et al., "Flight of an aeroplane with solid-state propulsion," *Nature*, vol. 563, no. 7732, pp. 532–535, Nov. 2018.
[7] V. Y. Khomich and I. E. Rebrov, "In-atmosphere electrohydrodynamic propulsion aircraft with wireless supply onboard," *J. Electrostatics*, vol. 95, pp. 1–12, Oct. 2018.
[8] E. D. Krauss, "Self contained ion powered aircraft," Patent U.S. 10 119 527 B2, Jun. 11, 2018.
[9] J. S. Townsend, "XI. The potentials required to maintain currents between coaxial cylinders," *London, Edinburgh, Dublin Phil. Mag. J. Sci.*, vol. 28, no. 163, pp. 83–90, Jul. 1914.
[10] A. Fridman and L. Kennedy, *Plasma Physics and Engineering*. New York, NY, USA: Taylor & Francis, 2004.
[11] J. Wilson, H. Perkins, and W. Thompson, "An investigation of ionic wind propulsion," NASA, Washington, DC, USA, Tech. Rep. NASA/TM-2009-215822, 2009.
[12] M. Belan, J. Baldo, O. Kahol, and D. Montenero, "Blade emitters for atmospheric ionic thrusters," *J. Phys. D: Appl. Phys.*, vol. 57, no. 19, May 2024, Art. no. 195201.
[13] M. Kaci, H. Ait Said, A. Laifaoui, M. Aissou, H. Nouri, and Y. Zebboudj, "Investigation on the corona discharge in blade-to-plane electrode configuration," *Brazilian J. Phys.*, vol. 45, no. 6, pp. 643–655, Dec. 2015.
[14] A. Ieta and M. Chirita, "Electrohydrodynamic propeller for in-atmosphere propulsion; rotational device first flight," *J. Electrostatics*, vol. 100, Jul. 2019, Art. no. 103352.
[15] D. S. Drew and S. Follmer, "High force density multi-stage electrohydrodynamic jets using folded laser microfabricated electrodes," in *Proc. 21st Int. Conf. Solid-State Sensors, Actuat. Microsyst. (Transducers)*, New York, NY, USA, Jun. 2021, pp. 54–57.
[16] M. Chirita and A. Ieta, "First rotary ionic engine with contra-rotating propellers," *J. Propuls. Power*, vol. 38, no. 6, pp. 893–900, Nov. 2022.
[17] E. Moreau, N. Benard, J.-D. Lan-Sun-Luk, and J.-P. Chabriat, "Electrohydrodynamic force produced by a wire-to-cylinder DC corona discharge in air at atmospheric pressure," *J. Phys. D: Appl. Phys.*, vol. 46, no. 47, Nov. 2013, Art. no. 475204.
[18] O. Kahol, M. Belan, M. Pacchiani, and D. Montenero, "Scaling relations for the geometry of wire-to-airfoil atmospheric ionic thrusters," *J. Electrostatics*, vol. 123, May 2023, Art. no. 103815.
[19] M. Belan, L. Arosti, R. Polatti, F. Maggi, S. Fiorini, and F. Sottovia, "A parametric study of electrodes geometries for atmospheric electrohydrodynamic propulsion," *J. Electrostatics*, vol. 113, Sep. 2021, Art. no. 103616.
[20] H. Xu, N. Gomez-Vega, D. R. Agrawal, and S. R. H. Barrett, "Higher thrust-to-power with large electrode gap spacing electroaerodynamic devices for aircraft propulsion," *J. Phys. D: Appl. Phys.*, vol. 53, no. 2, Jan. 2020, Art. no. 025202.
[21] A. Ieta, R. Ellis, D. Citro, M. Chirita, and J. D'Antonio, "Characterization of corona wind in a modular electrode configuration," in *Proc. ESA Annu. Meeting Electrostatics*, Jun. 2013, pp. 1–7.
[22] N. Gomez-Vega and S. R. H. Barrett, "Order-of-magnitude improvement in electroaerodynamic thrust density with multistaged ducted thrusters," *AIAA J.*, vol. 62, no. 4, pp. 1342–1353, Apr. 2024.
[23] M. Belan, R. Terenzi, S. Trovato, and D. Usuelli, "Effects of the emitters density on the performance of an atmospheric ionic thruster," *J. Electrostatics*, vol. 120, Nov. 2022, Art. no. 103767.
[24] J. Lemetayer, C. Marion, D. Fabre, and F. Plouraboué, "Multi-inception patterns of emitter array/collector systems in DC corona discharge," *J. Phys. D: Appl. Phys.*, vol. 55, no. 18, May 2022, Art. no. 185203.
[25] S. Arif, D. J. Branken, R. C. Everson, H. W. J. P. Neomagus, and A. Arif, "The influence of design parameters on the occurrence of shielding in multi-electrode ESPs and its effect on performance," *J. Electrostatics*, vol. 93, pp. 17–30, Jun. 2018.
[26] N. Gomez-Vega, H. Xu, J. M. Abel, and S. R. H. Barrett, "Performance of decoupled electroaerodynamic thrusters," *Appl. Phys. Lett.*, vol. 118, no. 7, Feb. 2021, Art. no. 074101.
[27] H. Xu, Y. He, and S. R. H. Barrett, "A dielectric barrier discharge ion source increases thrust and efficiency of electroaerodynamic propulsion," *Appl. Phys. Lett.*, vol. 114, no. 25, Jun. 2019, Art. no. 254105.
[28] T. Orrière, É. Moreau, and D. Z. Pai, "Electric wind generation by nanosecond repetitively pulsed microplasmas," *J. Phys. D: Appl. Phys.*, vol. 52, no. 46, Sep. 2019, Art. no. 464002.
[29] D. Lacoste, D. Pai, and C. Laux, "Ion wind effects in a positive DC corona discharge in atmospheric pressure air," in *Proc. 42nd AIAA Aerosp. Sci. Meeting Exhib.*, 2004, p. 354.
[30] C. Guerra-Garcia, N. C. Nguyen, T. Mouratidis, and M. Martinez-Sanchez, "Corona discharge in wind for electrically isolated electrodes," *J. Geophys. Res., Atmos.*, vol. 125, no. 16, Aug. 2020, Art. no. e2020JD032908.
[31] S. Grosse, N. Benard, and E. Moreau, "Electroaerodynamic thrusters: Influence of a freestream on the current, ionic wind, and force produced by a DC corona discharge," *J. Electrostatics*, vol. 130, Aug. 2024, Art. no. 103950.
[32] C. E. D. Riboldi et al., "Preliminary sizing of high-altitude airships featuring atmospheric ionic thrusters: An initial feasibility assessment," *Aerospace*, vol. 11, no. 7, p. 590, Jul. 2024.

Davide Usuelli received the M.Sc. degree in aerospace engineering from Politecnico di Milano, Milan, Italy, in 2022, where he is currently pursuing the Ph.D. degree in an atmospheric application for plasma EHD thruster.

He attended the Research Master course at the von Karman Institute for Fluid Dynamics, Sint-Genesius-Rode, Belgium, from 2022 to 2023.

Raffaello Terenzi received the M.Sc. degree in aerospace engineering from Politecnico di Milano, Milan, Italy, in 2022, where he is currently pursuing the Ph.D. degree in atmospheric application for plasma EHD thruster.

He attended the Research Master course at the von Karman Institute for Fluid Dynamics, Sint-Genesius-Rode, Belgium, from 2022 to 2023.

Stefano Trovato received the M.Sc. degree in aerospace engineering from Politecnico di Milano, Milan, Italy, in 2022, where he is currently pursuing the Ph.D. degree in atmospheric application for plasma EHD thruster.

He attended the Research Master course at the von Karman Institute for Fluid Dynamics, Sint-Genesius-Rode, Belgium, from 2022 to 2023.

Marco Belan received the M.Sc. degree (Hons.) in physics from Universitá di Torino, Turin, Italy, in 1991, and the Ph.D. degree in aerospace engineering from Politecnico di Torino, Turin, in 1995.

Since 1999, he has been an Associate Professor with the Dipartimento di Scienze e Tecnologie Aerospaziali of Politecnico di Milano, Milan, Italy. He also works in the field of applied mathematics, dealing with modeling of the laboratory studies above. His research interests include nonequilibrium plasma (plasma–gas flow interactions, ionic propulsion, systems for gas ionization, and plasma generation) and experimental fluid mechanics (flow control, drag reduction techniques, low pressure and vacuum systems technology, evolution of free hypersonic jets, wind engineering of bluff bodies, and design of wind tunnel components).

Open Access funding provided by 'Politecnico di Milano' within the CRUI CARE Agreement